

# THz higher-order topological photonics in Ge-on-Si heterostructures

Ian Colombo, Pietro Minazzi, Emiliano Bonera, Fabio Pezzoli\* and Jacopo Pedrini

Department of Materials Science and BiQuTe, University of Milano-Bicocca,  
via R. Cozzi 55, 20125 Milan (Italy)

\* [fabio.pezzoli@unimib.it](mailto:fabio.pezzoli@unimib.it)

## Abstract

We design germanium-based higher-order topological cavities for terahertz applications by breaking the symmetry of a two-dimensional photonic crystal following the Su-Schrieffer-Heeger model. Calculations demonstrate the parity inversion of the electric field in differently deformed unit cells. The interface between domains of opposite topology presents edge and corner modes. The former are chiral, locking light propagation to its helicity. The latter prove that Ge-based structures can be used as high-order topological photonic crystals. These findings can accelerate the development of Si-photonics components working in a spectral range of high technological interest.



Copyright I. Colombo *et al.*

This work is licensed under the Creative Commons

[Attribution 4.0 International License](https://creativecommons.org/licenses/by/4.0/).

Published by the SciPost Foundation.

Received 27-11-2023

Accepted 03-06-2024

Published 04-07-2024

doi:[10.21468/SciPostPhysCore.7.3.039](https://doi.org/10.21468/SciPostPhysCore.7.3.039)



Check for  
updates

---

## Contents

<b>1</b>	<b>Introduction</b>	<b>1</b>
<b>2</b>	<b>Results and discussion</b>	<b>2</b>
<b>3</b>	<b>Conclusions</b>	<b>8</b>
<b>A</b>	<b>Role of the {111} facets</b>	<b>9</b>
<b>B</b>	<b>Details on the computational method</b>	<b>9</b>
<b>C</b>	<b>Bandstructure of the PC as a function of <math>d</math></b>	<b>12</b>
	<b>References</b>	<b>12</b>

---

## 1 Introduction

The comprehension and exploitation of the topological properties of matter led to the emergence of research on topological insulators [1] and their photonic analogs, known as topo-

logical photonic crystals (TPC) [2, 3]. TPCs have been shown to be promising for the fabrication of photonic integrated circuits thanks to exceptional features, e.g., directional and chiral light propagation [4–6], strong resistance to sharp bends [7], and mathematical protection from defect-induced scattering [8]. These properties are indeed expected to facilitate the implementation of advanced photonic components such as directional, polarization-dependent waveguides [9–11], resonators [12], drop-filters [13], and topological lasers. [7, 14, 15]

Lately, higher-order topology has been gaining attention in photonics research. In contrast to conventional topological insulators, higher-order topological insulators (HOTI) present conductive states that are more than one dimension lower than the insulating state [16, 17]. This has led to the concept of special two-dimensional (2D) TPCs, which can feature unusual zero-dimensional (0D) corner states in addition to the conductive one-dimensional (1D) hinge modes. The potential to exploit HOTIs to fully confine the electromagnetic field at a 0D corner and topologically protect it from undesired losses is fundamentally intriguing and strongly appealing for applications, particularly because it might drastically boost lasing emission and improve spectral purity [14].

Although crystals with a trivial photonic band structure have already found applications in the terahertz (THz) [18, 19], the extension of HOTIs into such frequency range has been limited thus far. The interest in this spectral regime comes from the inherent capacity to stream high-frequency wide-bandwidth data [20]; a characteristic that offers significant prospects for the advancement of wireless communication networks beyond existing 5G standards [21, 22]. In addition to telecommunications, THz waves can have far-reaching consequences in various fields, including quantum information [21–23], non-destructive imaging [24, 25], biological sensing and diagnostics [26, 27], security and defense [28, 29]. The development of efficient THz photonic components and devices is thus a compelling task where TPC and HOTIs can provide a leap forward with novel and yet untapped capabilities.

Another crucial factor in achieving this ambitious goal is the choice of materials platform that can favor an industrial takeover while being, at the same time, suitable for the THz regime. Germanium stands out as a solution to these two problems since it offers a transparency window that is spectrally broad [30, 31], while being already present in microelectronic and photonic foundries. Ge-based high-quality photonic crystals (PC) can be indeed created using conventional lithography and vertical etching of thin Ge-on-Si films [32–34] or by exploiting self-assembly of Ge crystals directly on top of patterned Si substrates [35]. This can result in high-volume production and opens the route toward monolithic integration of THz photonic components into Si chips.

So far, literature reports have shown that Ge-on-Si heterostructures host promising, albeit non-topological, photonic properties in the near-infrared region of the electromagnetic spectrum [36–38]. To unfold the Ge potential in exhibiting HOTI states in the THz regime, we employ the finite elements method (FEM) to investigate photonic and topological properties including the emergence of a photonic band gap (PBG) and the topology-induced spatial confinement and directional propagation of light. In this work, we will concentrate on the model system offered by the self-assembly of micron-sized Ge-on-Si rods. Their typical in-plane arrangement can seemingly mimic 2D TPCs with a square geometry [14, 39–43] and their distinct optical properties [44–48] can possibly expedite the practical realization of future, integrated HOTI devices.

## 2 Results and discussion

Figure 1a shows the layout of a typical microstructure consisting of Ge-on-Si microcrystals. To determine the photonic bandstructure of the 2D lattice as close as possible to the experimental

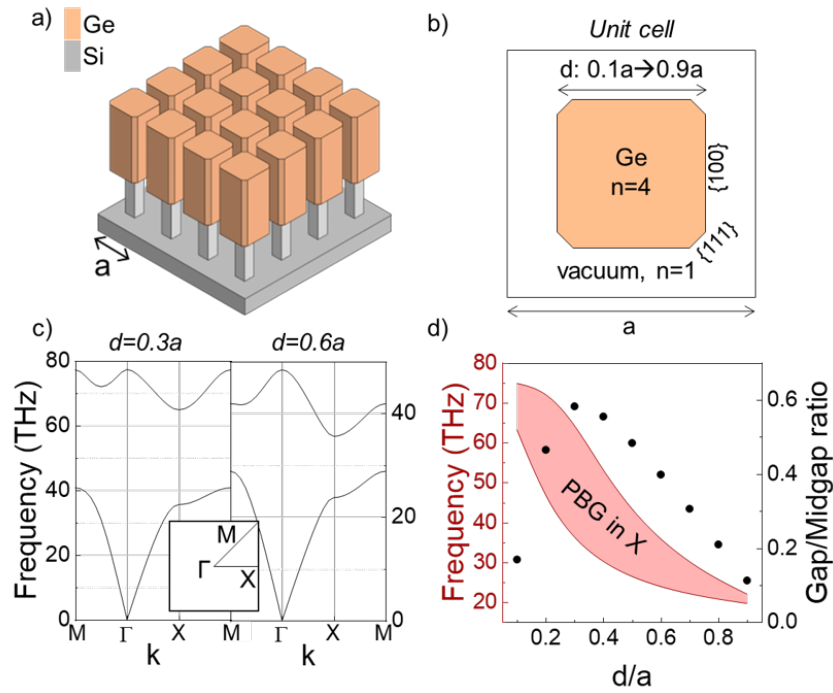


Figure 1: a) Sketch of the modeled photonic crystal (PC) based on a Ge (orange) on Si (grey) heterostructure (not to scale) [37]. The lattice parameter is  $a$ . b) Scheme of the simulated unit cell of the PC. c) Simulated bandstructure of the PC calculated using finite element method for a Ge crystal size  $d = 0.3a$  (left) and  $d = 0.6a$  (right). Inset: Irreducible Brillouin Zone of the square lattice with high symmetry points indicated. d) Size of the photonic bandgap (PBG) calculated in the  $X$  point of the bandstructure (red shaded area) and gap/midgap ratio (black dots) as a function of  $d$ .

ones [37], we simulated a unit cell composed of a pseudo-octagonal Ge microcrystal, featuring both  $\{100\}$  and  $\{111\}$  facets surrounded by vacuum. The  $\{111\}$  facets are sub-wavelength and their role on determining the photonic bandstructure of the crystal is negligible, as shown in Figure 5 in Appendix A, but they were included in the computational model for the sake of accurately simulating the results of fabrication. The lattice parameter is  $a = 2 \mu\text{m}$  to ensure experimental feasibility with conventional fabrication processes [37]. The size  $d$  of the Ge microcrystal was varied in the FEM calculations between  $0.1a$  and  $0.9a$ . The refractive index of Ge has been extracted from the literature [49] and is  $n \sim 4$ , corresponding to the value measured in the THz region of the electromagnetic spectrum, where the extinction coefficient is zero and  $n$  itself can be considered constant for the purposes of the calculations. The geometry of the unit cell, together with the structure parameters, is reported in Figure 1b.

We performed a FEM simulation of the system eigenfrequencies with Comsol Multiphysics [50, 51], using Floquet periodicity and varying the size  $d$  of the microcrystal to gather information on the optimal geometric parameters of the PC. The simulation was performed for the out-of-plane electric field configuration, also known as transverse magnetic (TM) modes. Further details on the simulation methods are reported in Appendix B. The simulation sweeps the wavevector  $k$  along high symmetry directions in the irreducible Brillouin Zone (IBZ), yielding the photonic bandstructure that is reported in Figure 1c for two values of  $d$ , namely  $d = 0.3a$  and  $d = 0.6a$ , corresponding to a microcrystal lateral size of 600 nm and 1200 nm, respectively. The calculated bandstructures for every value of  $d$  are reported in Figure 9 in Appendix C. The bandstructures present a large PBG in the THz region of the electromagnetic spectrum.

The bandstructures have similar shapes for different values of  $d$ , but its increase shifts the energy bands towards lower frequencies and apparently shrinks the amplitude of the PBG as shown in Figure 1d, which reports the size of the PBG at the X high-symmetry point of the IBZ as a function of  $d$ . The size of the gap increases with  $d$  and then decreases until it is almost negligible. This behavior is expected in 2D PCs dominated by a high refractive index material [52]. To compare the size of the PBG between the different structures, we normalized the bandgap to the midgap frequency. This renormalization method allows us to compare the relative amplitude of the PBG in structures with different geometries [52]. The calculation of the gap/midgap ratio in our case yields that the structure with the largest bandgap is that with  $d = 0.3a$ . Hereafter we refer to this specific value of  $d$ .

It should be noted that the photonic properties of the simulated system depend on the specific value of the lattice parameter  $a$ . However, the scaling invariance allows one to rigidly shift the energy of the PBG towards lower (higher) frequencies just by fabricating larger (smaller) unit cells. This powerful property provides great flexibility because it allows structures with a PBG in resonance with a desired frequency, e.g., the emission frequency of a quantum cascade structure. There are reports in the literature [53, 54] showing Ge/SiGe MQWs with interband emission at  $\sim 30$  THz, a value that can already be reached with the PC described in Figure 1, e.g. for  $d = 0.8a$ . The structure can be further optimized by setting  $d = 0.3a$ , where the PBG is the largest, and increasing the lattice parameter  $a$  by a factor  $\sim 2$ .

The 2D lattice composed of the semiconductor microcrystals can be seen as the periodic repetition of two different unit cells. The two structures can be considered the extreme case of a photonic extension of a 2D Su-Schrieffer-Heeger (SSH) lattice [40, 55, 56], where a unit cell composed of four elements equidistant from both the center and the vertex of the cell is distorted, as shown in Figure 2. The first unit cell has a microcrystal with lateral size  $d$  at the center of the cell, as shown in Figure 1b or Figure 2a, and will from now on be referred to as *compressed*. The other structure consists of four quarters of a microcrystal with a width  $\frac{d}{2}$  placed at the corners of the cell, as shown in Figure 2c. We will refer to this structure as *expanded*. The *equidistant* unit cell structure is reported in Figure 2b.

The bandstructures of the described lattices are reported in Figure 2d-f. The one of the *equidistant* PC (reported in Figure 2e) is gapless and shows a pseudo-Dirac point at the M and X high-symmetry points. The deformation of the unit cell opens a gap, as expected in the SSH model, and yields two identical photonic bandstructures for the *compressed* and *expanded* PCs. It is important to highlight that in a SSH model the band dispersion does not change with the inversion of the intra- and inter-cellular distances between the elements composing the unit cell, but the symmetry of the eigenfunctions is different, as they possess opposite parity [40, 56]. The topological invariant in SSH-like 2D photonic crystals like those described in this work can be classified by the Zak phase [40, 57], which is basically the integral of the Berry connection on the Brillouin Zone. In some works [40] the bulk polarization  $P$  is discussed instead of the Zak phase  $\phi_Z$ , but the two are simply related by  $\phi_Z = 2\pi P$ . The values of the Zak phase form a  $\mathbb{Z}_2$  index in  $C_4$ -symmetric topological crystals such as the one described in our work and can only take the values 0 or  $\pi$  for each direction for trivial or non-trivial topologies, respectively [41, 58]. It is known from the literature [40, 41] that in structures akin to those described in this work, the Zak phase for the directions  $(x, y)$  is  $(0, 0)$  for the *compressed* structure and  $(\pi, \pi)$  for the *expanded* structure, meaning that the structures are topologically trivial and nontrivial, respectively. To gather further insights on the bandstructure of the *expanded* and *compressed* PCs, we calculated the out-of-plane electric field distribution  $E_z$  (TM mode) for such unit cells. Particularly, we investigate the  $E_z$  distribution at the X point of the bandstructure, where the PBG opens up. The  $E_z$  distribution maps are reported in Figure 2g,h. Here, the *compressed* PC presents an even  $E_z$  distribution in the lower band and an odd distribution in the high-energy band. The opposite occurs in the *expanded* structure. This parity

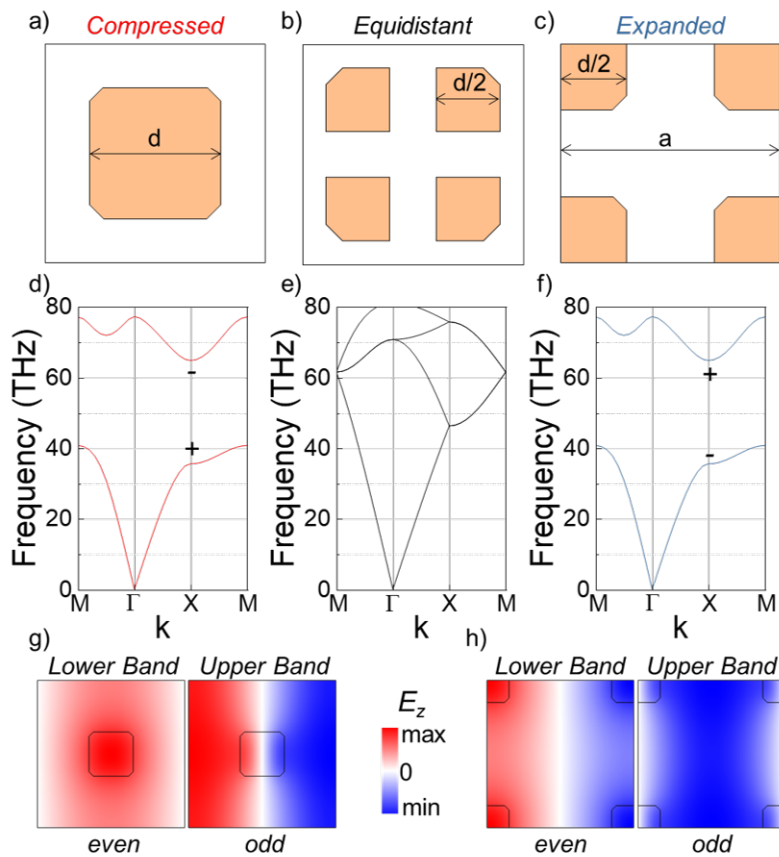


Figure 2: Scheme of the unit cell, simulated photonic bandstructure, and electromagnetic field distribution for the *compressed* (a,d,g), *equidistant* (b,e) and *expanded* (c,f,h) PCs when the lateral size of the Ge crystal  $d$  equals 0.3 times the lattice parameter  $a$ . The out-of-plane component of the electromagnetic field (TM mode) is computed at the X point of the IBZ. The parity of the wavefunction acts as a pseudospin, and the symmetry inversion (indicated by the + and -) between the *compressed* and the *expanded* crystals is the fingerprint of a topological phase transition.

inversion confirms the equivalence of the two PC structures to a 2D SSH model. Therefore, the *compressed* and *expanded* PC belongs to distinct topological phases, where the parity of the bands can be considered as the topological invariant. In particular, the *compressed* structure is an ordinary insulator, while the *expanded* is topologically nontrivial. It is worth noting that the definition of the unit cells does not affect the eigenvalues of the system, i.e., the photonic bandstructure: the *compressed* and *expanded* cells generate the same bulk (infinite) structure. In other words, when the PC has no boundaries, the *compressed* and *expanded* cells can be mapped one into the other, and the choice of the repeating unit does not yield differences in light propagation. Yet the eigenfunctions, i.e., the electromagnetic field distribution associated to a given eigenvalue, can differ. More specifically, the degree of freedom that changes between the two structures is the parity of  $E_z$ , which is reflected by the change in the Zak phase from  $(0, 0)$  in the *compressed* cell to  $(\pi, \pi)$  in the *expanded* cell. While this property does not manifest itself in the bulk, it has a physical consequence when an interface is realized between the two topologically distinct domains. Indeed, the presence of a junction that acts as a boundary implies a closing gap to connect the states having the same parity [59].

This is one of the fingerprints of a topological transition and is generally referred to as bulk-edge correspondence, i.e., the emergence of spatially confined guided modes at the boundary

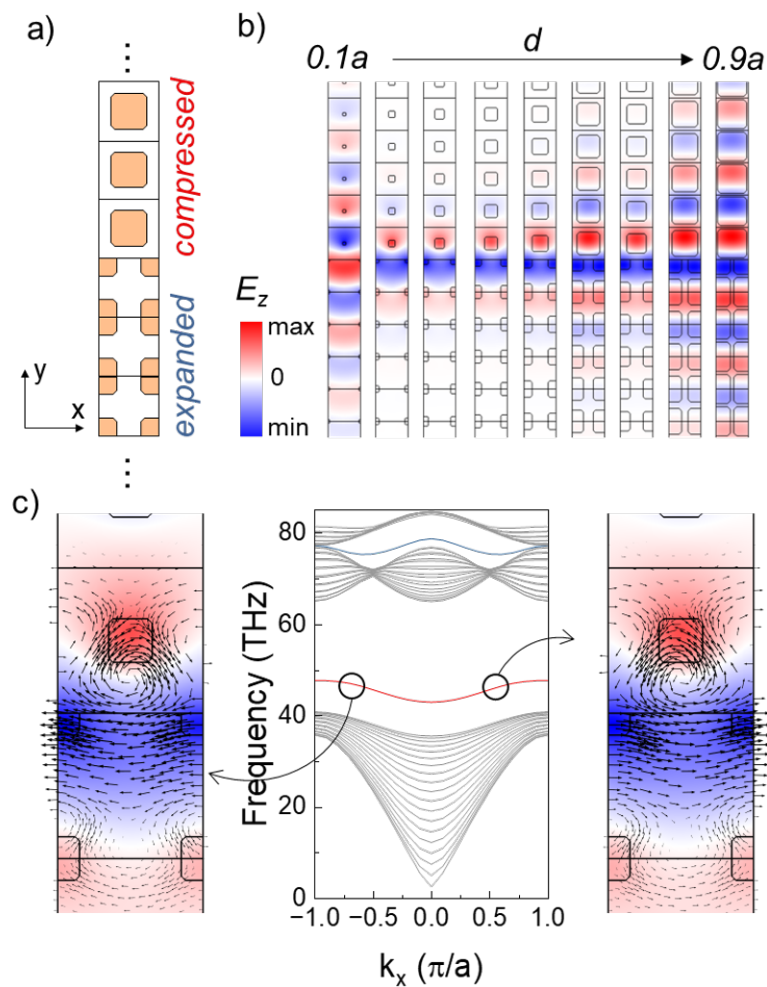


Figure 3: a) Schematics of a supercell consisting of a line interface between a *compressed* and *expanded* PCs ( $d = 0.3a$ ). b) Spatial distribution of the out-of-plane component of the electromagnetic field ( $E_z$ ) in the supercell as a function of the lateral size of Ge  $d$ . The supercells are stacked horizontally as  $d$  increases from  $0.1a$  to  $0.9a$ , where  $a$  is the lattice parameter. c) Calculated bandstructure of the supercell along the  $x$  direction. The bandstructure presents bulk bands (grey) with two sizeable gaps in which localized modes are present (red and blue curves). The modes are confined at the interface of the two regions of the PCs. The arrows overlaid on the electromagnetic field distribution underline the directionality of the propagation.

between two domains with different band topology [1, 5, 7, 60, 61]. Figure 3a reports the schematic of an interface between the two PCs characterized by distinct topological invariants. For its characterization we designed a so-called *supercell* composed of a ribbon of 20 unit cells where the top (bottom) 10 unit cells are *compressed* (*expanded*). In other words, the top half of the supercell is an ordinary insulator, while the bottom half is topologically nontrivial. The FEM simulation of this structure is performed with periodic conditions along the  $x$  direction, and the eigenfrequencies are calculated as a function of  $k_x$ , from  $-\frac{\pi}{a}$  to  $\frac{\pi}{a}$ . A perfectly matched layer is used as the boundary condition for the top and bottom of the ribbon to simulate an infinite PC. The results of the FEM simulations are shown in Figure 3b,c. The bandstructure in Figure 3c presents a large number of bulk modes and two energy gaps, the larger of which covers the interval between 41 and 65 THz, while a second, non complete one is at around 75 THz. For the scope of this work, we focus on the full PBG at lower energy. The bandgap

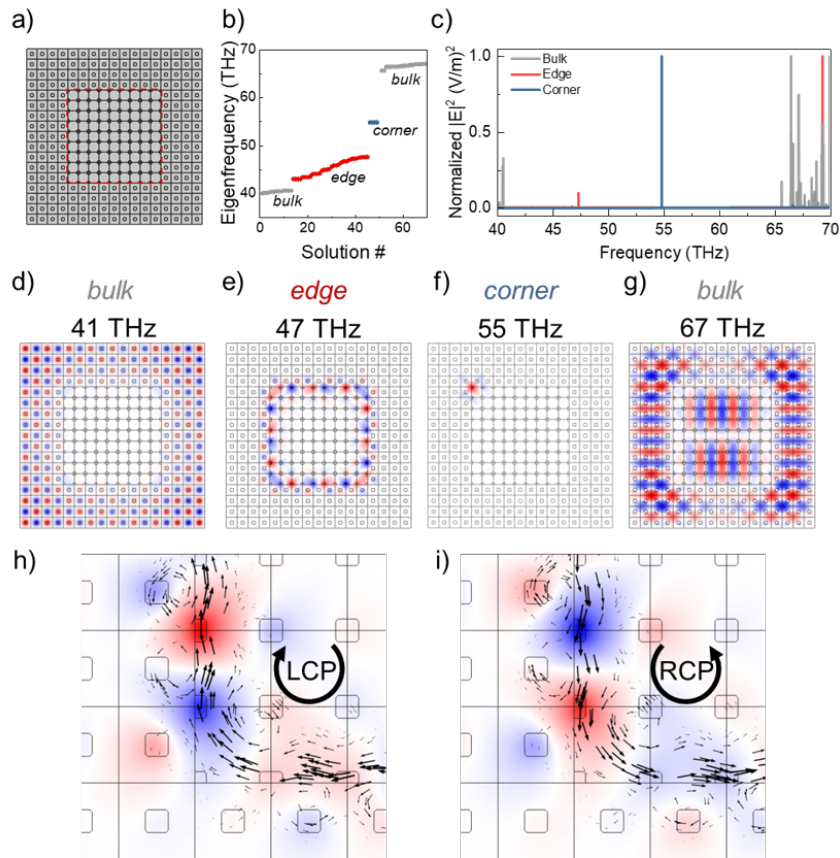


Figure 4: a) Schematics of a resonator composed of a square interface between an *expanded* PC surrounded by a *compressed* PC ( $d = 0.3a$ ). The interface is marked with a red dashed line. b) Eigenfrequency values of the resonator as a function of the solution number. Four groups can be identified that correspond to bulk modes (low- and high-energy, grey), edge (red), and corner (blue) modes. c) Normalized field intensity as a function of the frequency, highlighting the bulk, edge and corner modes. d-g) Distribution of the out-of-plane component of the electric field at four significant frequencies corresponding to a low-energy bulk mode (d), edge mode (e), corner mode (f), and a high-energy bulk mode (g). h,i) Electromagnetic field  $E_z$  distribution at the bottom left corner of the resonator, when the resonator is excited with left (h) and right (i) circularly polarized light. The arrows at the interface between the topologically distinct regions are the Poynting vectors, highlighting a direct correspondence between light polarization and the direction of propagation.

frequencies are the same as those calculated for the bulk unit cells along the  $\Gamma - X$  direction (see Figure 2). The presence of a single mode in the PBG, located at  $\sim 45$  THz, is a fingerprint of the interface of two phases with a different topological invariant. Such a mode is spatially localized at the interface of the two domains, as is shown by the plot of  $E_z$  (see Figure 3b,c), with the electric field mostly penetrating the high-index structure. The arrows overlaid on the  $E_z$  map in Figure 3c are the local Poynting vectors that represents the direction of propagation of the electromagnetic wave. The representation of the Poynting vector allows us to underline the presence of unidirectional propagating modes, which can be selectively coupled through helical excitation [3, 5, 62]. Figure 3b shows that when  $d$  is varied the imbalance between the air and Ge fractions affects the confinement of the edge mode, so that the field is almost perfectly localized within the two interfacial unit cells only for  $d$  ranging from  $0.2a$  to  $0.5a$ .

The demonstration of the presence of optical modes at the interface between domains suggests a possible application of Ge-on-Si photonic architectures as on-chip THz waveguides in topological circuits. We can further extend our results by designing a 2D device that could also exploit the generation of higher-order topological modes at the intersection between such hinge modes. Figure 4a introduces a resonator composed of a square of the *expanded* PC having a side of 9-unit cells, surrounded by a cladding frame consisting of 4-unit cells of the *compressed* PC defining an interface that supports the mode described in Figure 3. The solutions of the eigenvalue analysis for the resonator are separated in four well-defined frequency regions, as shown in Figure 4b,c. The nature of these modes can be determined by analyzing the electric field distribution, as shown in Figure 4d-g. The electromagnetic field maps for solutions for frequencies  $< 41$  THz (see Figure 4d) and  $> 65$  THz (see Figure 4g) clearly demonstrate the bulk nature of the modes, that permeate vast regions of the PC. In the frequency range pertaining to the PBG two well separated sets of solutions are present at  $\sim 47$  THz and at 55 THz. First, we focus on the four degenerate modes at 55 THz that dominate the energy density spectrum reported in Figure 4c. The map of the electric field distribution, reported in Figure 4f, shows that these are extremely localized 0D corner modes. Their existence demonstrates that the structure described in this work is a higher-order TPC characterized by a bulk-edge-corner correspondence [63]. Moreover, localized corner modes are extremely interesting for their strong confinement properties and can be exploited for their possible applications to devices that need high-quality factor resonators such as light emitters, sensors, and non-linear systems [40, 41, 64, 65]. The resonator introduced in this work is an initial demonstration of a topological device utilizing group-IV semiconductors, which shows promise for use in high-quality factor emitters that are directly integrated into the Si platform.

We now focus on the lower energy modes, found at frequency around 47 THz. The electromagnetic field distribution shows that these are edge modes confined at the interface between the trivial and topological PC structures. Their study can give further insight on the topological properties of the PC and how they influence the propagation of light at the interface between the two topologically-distinct domains. As described above, a characteristic property of TPCs is the directional propagation of light, which is related to its degree of circular polarization. To demonstrate this feature, we simulated the propagation of circularly polarized light by using an array of phased dipoles localized at the interface between the topologically distinct regions [66]. The overlay of the Poynting vector on the electromagnetic field map, shown in Figure 4h-i, demonstrates how the propagation is strongly directional and locked to the degree of circular polarization, allowing chiral propagation at the interface of the PCs in the THz range.

### 3 Conclusions

We demonstrated the possibility of achieving higher-order topological effects in the THz regime in a PC composed of group IV heteroepitaxial microstructures. Such a HOTIs can be utilized for the development of elemental components of photonic circuitries such as resonators and waveguides. By combining Ge-based heterostructures with the intrinsic scalability of PCs one can obtain devices working in a wide range of frequencies, possibly from mid-infrared to the THz. Furthermore, the capacity to embed THz emitters in the microstructures in the form of Ge/SiGe quantum wells might open a pathway to realize integrated, topological lasers with a small footprint and high throughput that operate within technologically relevant spectral regions.

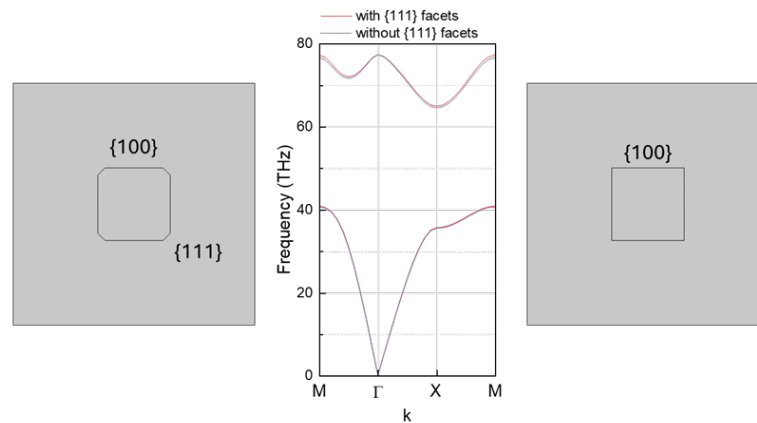


Figure 5: Photonic bandstructure for a *compressed* unit cell with the Ge element presenting both  $\{100\}$  and  $\{111\}$  facets (left) compared to one with only  $\{100\}$  facets (right).

## Acknowledgments

The authors thank A. Marzegalli for technical assistance and L. Miglio for fruitful discussions.

**Funding information** This work has been funded by the European Union’s Horizon Europe Research and Innovation Programme under agreement 101070700. Support from PNRR MUR project PE0000023-NQSTI is also acknowledged. J.P. acknowledges financial support from FSE REACT-EU (grant 2021-RTDAPON-144).

## A Role of the $\{111\}$ facets

The role of the microcrystal faceting was investigated by comparing the photonic bandstructure of the unit cell shown in Figure 1 to that of the same unit cell but with the Ge microcrystal only possessing  $\{100\}$  facets, i.e. a perfect square. Figure 5 shows that the bandstructures are almost identical, if not for a negligible red-shift for the structure without  $\{111\}$  facets. This is most likely determined by the slightly larger fraction of the unit cell that is occupied by the high refractive index material, which is known to shift the energy gap towards lower energy. This analysis shows that the role of the  $\{111\}$  facets is negligible, as expected by strongly sub-wavelength fine-structuring of the elements composing the photonic crystal.

## B Details on the computational method

The photonic simulations were performed with Comsol Multiphysics 6.1, by using the *wave optics module*. The chosen physics was *electromagnetic wave, frequency domain* and we performed an *eigenfrequency* analysis.

### Eigenfrequency calculation for the unit cells

The solutions were calculated for the out-of-plane electromagnetic wave (TM mode) by using Floquet periodic boundary conditions both in the x and y direction. The wave vectors  $k_x$  and

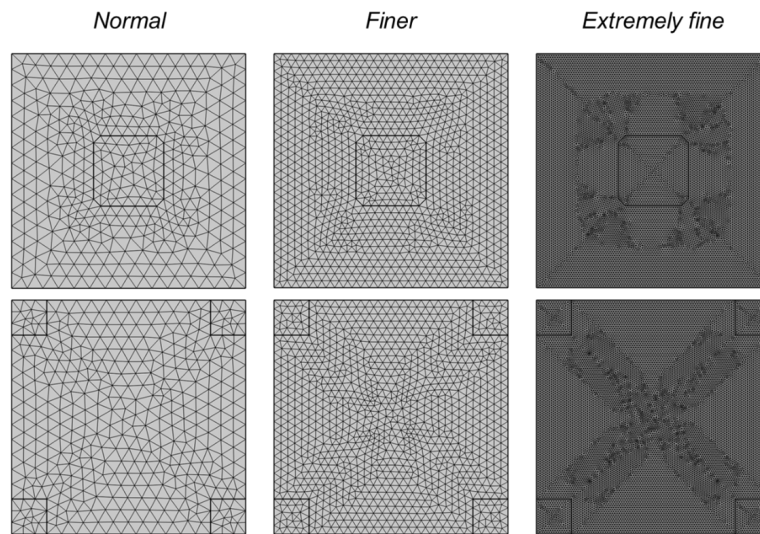


Figure 6: Meshed unit cells with the parameters described in Table 1.

$k_y$  were swept by mapping the high symmetry directions of the square irreducible Brillouin Zone (see the inset in Figure 1c) with a parameter  $k$ , in such a way that the high symmetry points M,  $\Gamma$ , X, and M correspond to  $k = 0, k = 1, k = 2, k = 3$ , respectively. The parameter  $k$  was increased by 0.1 from 0 to 3 for a total of 32 simulated wavevector values. For the supercell, the solutions were calculated for the out-of-plane electromagnetic wave (TM mode) by using Floquet periodic boundary conditions only in the x direction. The wave vector  $k_x$  was swept from  $-\pi/a$  to  $\pi/a$ . The  $k_x$  parameter was increased by  $0.1 \times \pi/a$ . For the resonator, the solutions were calculated for the out-of-plane electromagnetic wave (TM mode) by using absorbing boundaries to simulate infinite propagation.

### Mesh size

The simulations were performed with a free triangular mesh with the *finer* setting, corresponding to a mesh of triangular elements with maximum element size of 78 nm and a minimum element size of 0.25 nm. The parameters were chosen to have a good trade-off between computational speed and accuracy of the simulation. Nevertheless, by increasing or decreasing the mesh size to the *normal* or *extremely fine* values, the simulation yields the same results. The parameters for the meshes that were tested are reported in Table 1, while the meshed unit cells are shown in Figure 6 and the calculated bandstructures for each meshed cell are shown in Figure 7.

### Error and convergence

A sample convergence plot for the calculation of the photonic bandstructure of the *compressed* unit cell, with the *finer* mesh described in Table 1 is reported in Figure 8. The plot shows the

Table 1: Parameters of three meshes tested for the computational work.

	Normal	Finer	Extremely fine
Max. element size (nm)	134	74	20
Min. element size (nm)	0.60	0.25	0.04
Max. element growth rate	1.3	1.25	1.1
Curvature factor	0.3	0.25	0.2

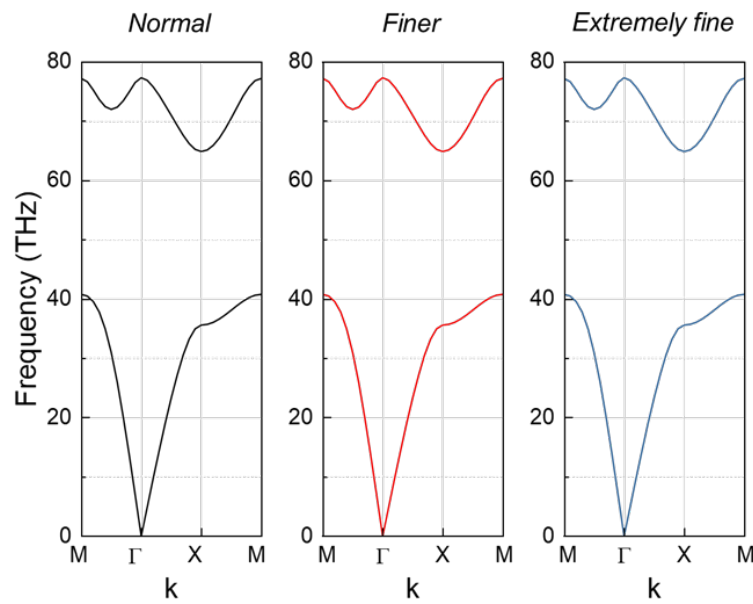


Figure 7: Photonic bandstructure calculated with the three meshes described in table 1.

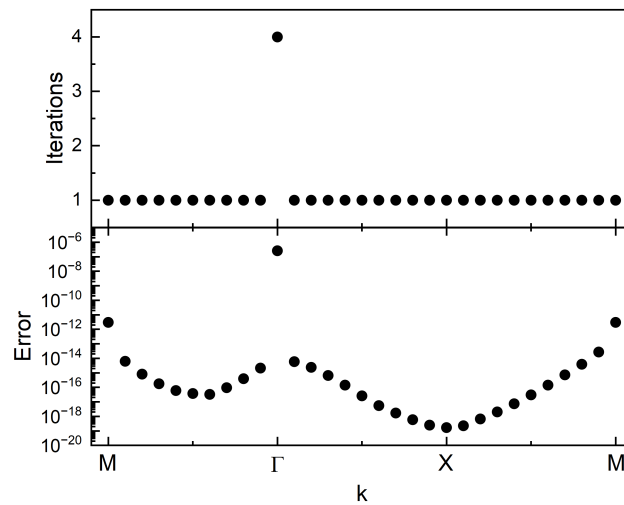


Figure 8: Convergence plot for the calculation of the bandstructure of the *compressed* unit cell, performed with *finer* mesh settings described in Table 1. Top: number of iterations needed to reach convergence. Bottom: error of the calculation when convergence is reached.

number of iterations needed to reach convergence for each  $k$  point of the bandstructure. The calculation error is generally around or lower than  $10^{-15}$  and is reached at the first iteration of the eigenfrequency calculation. This is not true for the  $\Gamma$  point of the bandstructure that, having an eigenfrequency close to zero, is less accurate and needs four iterations to reach an error of  $10^{-7}$ . Nevertheless, it is important to note that in the X point of the bandstructure, i.e. where the topological inversion occurs, the error is of the order of  $10^{-19}$ .

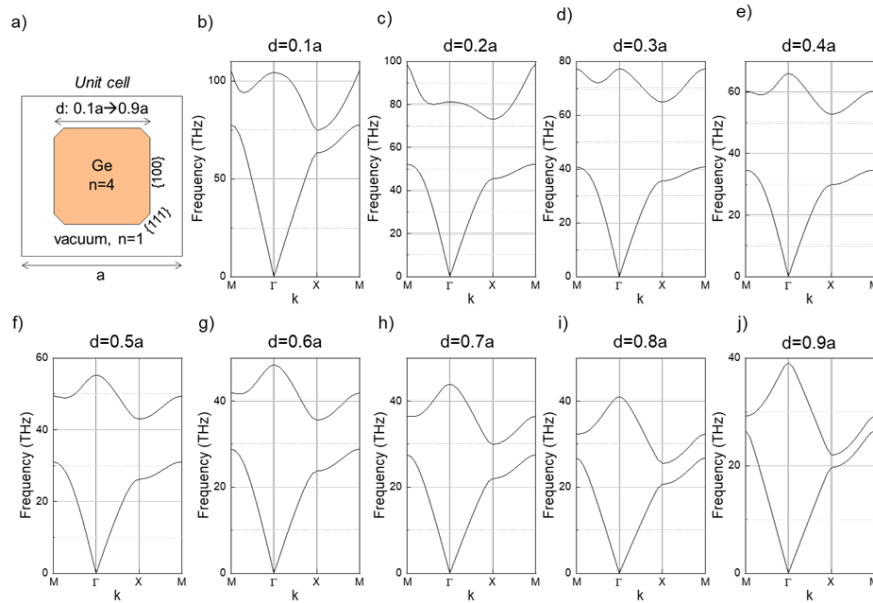


Figure 9: Photonic bandstructure calculated with the finite element method for the PC described in a) as a function of the ratio between the size of the Ge element  $d$  and the lattice parameter  $a$ .

### C Bandstructure of the PC as a function of $d$

The bandstructure of the *compressed* unit cell was investigated as a function of the microcrystal size  $d$ , from  $d = 0.1a$  to  $d = 0.9a$ . The results of such investigation are reported in Figure 9. A full PBG is present only for  $0.2a < d < 0.7a$ . However, the PBG in X, point of the IBZ where the topological inversion occurs, is present for every value of  $d$ .

The increase of the average refractive index of the unit cell, that is obviously proportional to the size of the microcrystal, shifts the photonic bandstructure towards lower frequencies, with a PBG in X centered at  $\sim 70$  THz for  $d = 0.1a$  and at  $\sim 21$  THz for  $d = 0.9a$ .

### References

- [1] M. Z. Hasan and C. L. Kane, *Colloquium: Topological insulators*, Rev. Mod. Phys. **82**, 3045 (2010), doi:[10.1103/RevModPhys.82.3045](https://doi.org/10.1103/RevModPhys.82.3045).
- [2] L. Lu, J. D. Joannopoulos and M. Soljačić, *Topological photonics*, Nat. Photon. **8**, 821 (2014), doi:[10.1038/nphoton.2014.248](https://doi.org/10.1038/nphoton.2014.248).
- [3] T. Ozawa et al., *Topological photonics*, Rev. Mod. Phys. **91**, 015006 (2019), doi:[10.1103/RevModPhys.91.015006](https://doi.org/10.1103/RevModPhys.91.015006).
- [4] P. Lodahl, S. Mahmoodian, S. Stobbe, A. Rauschenbeutel, P. Schneeweiss, J. Volz, H. Pichler and P. Zoller, *Chiral quantum optics*, Nature **541**, 473 (2017), doi:[10.1038/nature21037](https://doi.org/10.1038/nature21037).
- [5] L.-H. Wu and X. Hu, *Scheme for achieving a topological photonic crystal by using dielectric material*, Phys. Rev. Lett. **114**, 223901 (2015), doi:[10.1103/PhysRevLett.114.223901](https://doi.org/10.1103/PhysRevLett.114.223901).

- [6] J.-W. Dong, X.-D. Chen, H. Zhu, Y. Wang and X. Zhang, *Valley photonic crystals for control of spin and topology*, Nat. Mater. **16**, 298 (2016), doi:[10.1038/nmat4807](https://doi.org/10.1038/nmat4807).
- [7] Y. Zeng et al., *Electrically pumped topological laser with valley edge modes*, Nature **578**, 246 (2020), doi:[10.1038/s41586-020-1981-x](https://doi.org/10.1038/s41586-020-1981-x).
- [8] Z. Wang, Y. Chong, J. D. Joannopoulos and M. Soljačić, *Observation of unidirectional backscattering-immune topological electromagnetic states*, Nature **461**, 772 (2009), doi:[10.1038/nature08293](https://doi.org/10.1038/nature08293).
- [9] M. Jalali Mehrabad, A. P. Foster, R. Dost, E. Clarke, P. K. Patil, A. M. Fox, M. S. Skolnick and L. R. Wilson, *Chiral topological photonics with an embedded quantum emitter*, Optica **7**, 1690 (2020), doi:[10.1364/OPTICA.393035](https://doi.org/10.1364/OPTICA.393035).
- [10] Y. Yang, Y. F. Xu, T. Xu, H.-X. Wang, J.-H. Jiang, X. Hu and Z. H. Hang, *Visualization of a unidirectional electromagnetic waveguide using topological photonic crystals made of dielectric materials*, Phys. Rev. Lett. **120**, 217401 (2018), doi:[10.1103/PhysRevLett.120.217401](https://doi.org/10.1103/PhysRevLett.120.217401).
- [11] N. Parappurath, F. Alpeggiani, L. Kuipers and E. Verhagen, *Direct observation of topological edge states in silicon photonic crystals: Spin, dispersion, and chiral routing*, Sci. Adv. **6**, eaaw4137 (2020), doi:[10.1126/sciadv.aaw4137](https://doi.org/10.1126/sciadv.aaw4137).
- [12] M. Jalali Mehrabad, A. P. Foster, R. Dost, E. Clarke, P. K. Patil, I. Farrer, J. Heffernan, M. S. Skolnick and L. R. Wilson, *A semiconductor topological photonic ring resonator*, Appl. Phys. Lett. **116**, 061102 (2020), doi:[10.1063/1.5131846](https://doi.org/10.1063/1.5131846).
- [13] M. Jalali Mehrabad, A. P. Foster, N. J. Martin, R. Dost, E. Clarke, P. K. Patil, M. S. Skolnick and L. R. Wilson, *Chiral topological add-drop filter for integrated quantum photonic circuits*, Optica **10**, 415 (2023), doi:[10.1364/OPTICA.481684](https://doi.org/10.1364/OPTICA.481684).
- [14] C. Han, M. Kang and H. Jeon, *Lasing at multidimensional topological states in a two-dimensional photonic crystal structure*, ACS Photon. **7**, 2027 (2020), doi:[10.1021/acsp Photonics.0c00357](https://doi.org/10.1021/acsp Photonics.0c00357).
- [15] Y. Ota, R. Katsumi, K. Watanabe, S. Iwamoto and Y. Arakawa, *Topological photonic crystal nanocavity laser*, Commun. Phys. **1**, 86 (2018), doi:[10.1038/s42005-018-0083-7](https://doi.org/10.1038/s42005-018-0083-7).
- [16] F. Schindler, A. M. Cook, M. G. Vergniory, Z. Wang, S. S. P. Parkin, B. A. Bernevig and T. Neupert, *Higher-order topological insulators*, Sci. Adv. **4**, eaat0346 (2018), doi:[10.1126/sciadv.aat0346](https://doi.org/10.1126/sciadv.aat0346).
- [17] A. Dutt, M. Minkov, I. A. D. Williamson and S. Fan, *Higher-order topological insulators in synthetic dimensions*, Light Sci. Appl. **9**, 131 (2020), doi:[10.1038/s41377-020-0334-8](https://doi.org/10.1038/s41377-020-0334-8).
- [18] W. Withayachumnankul, M. Fujita and T. Nagatsuma, *Integrated silicon photonic crystals toward terahertz communications*, Adv. Opt. Mater. **6**, 1800401 (2018), doi:[10.1002/adom.201800401](https://doi.org/10.1002/adom.201800401).
- [19] R. A. S. D. Koala, M. Fujita and T. Nagatsuma, *Nanophotonics-inspired all-silicon waveguide platforms for terahertz integrated systems*, Nanophotonics **11**, 1741 (2022), doi:[10.1515/nanoph-2021-0673](https://doi.org/10.1515/nanoph-2021-0673).
- [20] T. Nagatsuma, G. Ducournau and C. C. Renaud, *Advances in terahertz communications accelerated by photonics*, Nat. Photon. **10**, 371 (2016), doi:[10.1038/nphoton.2016.65](https://doi.org/10.1038/nphoton.2016.65).

- [21] Y. Yang, Y. Yamagami, X. Yu, P. Pitchappa, J. Webber, B. Zhang, M. Fujita, T. Nagatsuma and R. Singh, *Terahertz topological photonics for on-chip communication*, Nat. Photon. **14**, 446 (2020), doi:[10.1038/s41566-020-0618-9](https://doi.org/10.1038/s41566-020-0618-9).
- [22] A. Kumar, M. Gupta, P. Pitchappa, N. Wang, M. Fujita and R. Singh, *Terahertz topological photonic integrated circuits for 6G and beyond: A perspective*, J. Appl. Phys. **132**, 140901 (2022), doi:[10.1063/5.0099423](https://doi.org/10.1063/5.0099423).
- [23] A. Leitenstorfer et al., *The 2023 terahertz science and technology roadmap*, J. Phys. D: Appl. Phys. **56**, 223001 (2023), doi:[10.1088/1361-6463/acbe4c](https://doi.org/10.1088/1361-6463/acbe4c).
- [24] K. Kawase, Y. Ogawa, Y. Watanabe and H. Inoue, *Non-destructive terahertz imaging of illicit drugs using spectral fingerprints*, Opt. Express **11**, 2549 (2003), doi:[10.1364/oe.11.002549](https://doi.org/10.1364/oe.11.002549).
- [25] C. Jansen et al., *Terahertz imaging: Applications and perspectives*, Appl. Opt. **49**, E48 (2010), doi:[10.1364/AO.49.000E48](https://doi.org/10.1364/AO.49.000E48).
- [26] P. H. Siegel, *Terahertz technology in biology and medicine*, IEEE Trans. Microw. Theory Tech. **52**, 2438 (2004), doi:[10.1109/TMTT.2004.835916](https://doi.org/10.1109/TMTT.2004.835916).
- [27] X. Yang, X. Zhao, K. Yang, Y. Liu, Y. Liu, W. Fu and Y. Luo, *Biomedical applications of terahertz spectroscopy and imaging*, Trends Biotechnol. **34**, 810 (2016), doi:[10.1016/j.tibtech.2016.04.008](https://doi.org/10.1016/j.tibtech.2016.04.008).
- [28] J. F. Federici, B. Schulkin, F. Huang, D. Gary, R. Barat, F. Oliveira and D. Zimdars, *THz imaging and sensing for security applications – Explosives, weapons and drugs*, Semicond. Sci. Technol. **20**, S266 (2005), doi:[10.1088/0268-1242/20/7/018](https://doi.org/10.1088/0268-1242/20/7/018).
- [29] Y. C. Shen, T. Lo, P. F. Taday, B. E. Cole, W. R. Tribe and M. C. Kemp, *Detection and identification of explosives using terahertz pulsed spectroscopic imaging*, Appl. Phys. Lett. **86**, 1 (2005), doi:[10.1063/1.1946192](https://doi.org/10.1063/1.1946192).
- [30] D. Marris-Morini et al., *Germanium-based integrated photonics from near- to mid-infrared applications*, Nanophotonics **7**, 1781 (2018), doi:[10.1515/nanoph-2018-0113](https://doi.org/10.1515/nanoph-2018-0113).
- [31] M. Montesinos-Ballester et al., *Optical modulation in Ge-rich SiGe waveguides in the mid-infrared wavelength range up to 11  $\mu\text{m}$* , Commun. Mater. **1**, 6 (2020), doi:[10.1038/s43246-019-0003-8](https://doi.org/10.1038/s43246-019-0003-8).
- [32] M. El Kurdi, S. David, X. Checoury, G. Fishman, P. Boucaud, O. Kermarrec, D. Bensahel and B. Ghyselen, *Two-dimensional photonic crystals with pure germanium-on-insulator*, Opt. Commun. **281**, 846 (2008), doi:[10.1016/j.optcom.2007.10.008](https://doi.org/10.1016/j.optcom.2007.10.008).
- [33] M. Schatzl et al., *Enhanced telecom emission from single group-IV quantum dots by precise CMOS-compatible positioning in photonic crystal cavities*, ACS Photon. **4**, 665 (2017), doi:[10.1021/acsp Photonics.6b01045](https://doi.org/10.1021/acsp Photonics.6b01045).
- [34] H.-J. Joo et al., *1D photonic crystal direct bandgap GeSn-on-insulator laser*, Appl. Phys. Lett. **119**, 201101 (2021), doi:[10.1063/5.0066935](https://doi.org/10.1063/5.0066935).
- [35] C. V. Falub et al., *Scaling hetero-epitaxy from layers to three-dimensional crystals*, Science **335**, 1330 (2012), doi:[10.1126/science.1217666](https://doi.org/10.1126/science.1217666).
- [36] J. Pedrini, P. Biagioni, A. Ballabio, A. Barzaghi, M. Bonzi, E. Bonera, G. Isella and F. Pezoli, *Broadband control of the optical properties of semiconductors through site-controlled self-assembly of microcrystals*, Opt. Express **28**, 24981 (2020), doi:[10.1364/oe.398098](https://doi.org/10.1364/oe.398098).

- [37] J. Pedrini, A. Barzaghi, J. Valente, D. J. Paul, G. Isella and F. Pezzoli, *Photonic band gap and light routing in self-assembled lattices of epitaxial Ge-on-Si microstructures*, Phys. Rev. Appl. **16**, 064024 (2021), doi:[10.1103/PhysRevApplied.16.064024](https://doi.org/10.1103/PhysRevApplied.16.064024).
- [38] V. Falcone et al., *Graphene/Ge microcrystal photodetectors with enhanced infrared responsivity*, APL Photon. **7**, 046106 (2022), doi:[10.1063/5.0082421](https://doi.org/10.1063/5.0082421).
- [39] Y.-H. He, Y.-F. Gao, H.-Z. Lin, M.-C. Jin, Y. He and X.-F. Qi, *Topological edge and corner states based on the transformation and combination of photonic crystals with square lattice*, Opt. Commun. **512**, 128038 (2022), doi:[10.1016/j.optcom.2022.128038](https://doi.org/10.1016/j.optcom.2022.128038).
- [40] B.-Y. Xie, G.-X. Su, H.-F. Wang, H. Su, X.-P. Shen, P. Zhan, M.-H. Lu, Z.-L. Wang and Y.-F. Chen, *Visualization of higher-order topological insulating phases in two-dimensional dielectric photonic crystals*, Phys. Rev. Lett. **122**, 233903 (2019), doi:[10.1103/PhysRevLett.122.233903](https://doi.org/10.1103/PhysRevLett.122.233903).
- [41] X.-D. Chen, W.-M. Deng, F.-L. Shi, F.-L. Zhao, M. Chen and J.-W. Dong, *Direct observation of corner states in second-order topological photonic crystal slabs*, Phys. Rev. Lett. **122**, 233902 (2019), doi:[10.1103/PhysRevLett.122.233902](https://doi.org/10.1103/PhysRevLett.122.233902).
- [42] K. Kim and K. Om, *Multiband photonic topological valley-Hall edge modes and second-order corner states in square lattices*, Adv. Opt. Mater. **9**, 1 (2021), doi:[10.1002/adom.202001865](https://doi.org/10.1002/adom.202001865).
- [43] M. Makwana, R. Craster and S. Guenneau, *Topological beam-splitting in photonic crystals*, Opt. Express **27**, 16088 (2019), doi:[10.1364/OE.27.016088](https://doi.org/10.1364/OE.27.016088).
- [44] F. Isa et al., *Highly mismatched, dislocation-free SiGe/Si heterostructures*, Adv. Mater. **28**, 884 (2015), doi:[10.1002/adma.201504029](https://doi.org/10.1002/adma.201504029).
- [45] F. Montalenti, F. Rovaris, R. Bergamaschini, L. Miglio, M. Salvalaglio, G. Isella, F. Isa and H. von Känel, *Dislocation-free SiGe/Si heterostructures*, Crystals **8**, 257 (2018), doi:[10.3390/cryst8060257](https://doi.org/10.3390/cryst8060257).
- [46] R. Bergamaschini, F. Isa, C. V. Falub, P. Niedermann, E. Müller, G. Isella, H. von Känel and L. Miglio, *Self-aligned Ge and SiGe three-dimensional epitaxy on dense Si pillar arrays*, Surf. Sci. Rep. **68**, 390 (2013), doi:[10.1016/j.surfrep.2013.10.002](https://doi.org/10.1016/j.surfrep.2013.10.002).
- [47] F. Pezzoli et al., *Ge crystals on Si show their light*, Phys. Rev. Appl. **1**, 044005 (2014), doi:[10.1103/PhysRevApplied.1.044005](https://doi.org/10.1103/PhysRevApplied.1.044005).
- [48] F. Pezzoli et al., *Disentangling nonradiative recombination processes in Ge micro-crystals on Si substrates*, Appl. Phys. Lett. **108**, 262103 (2016), doi:[10.1063/1.4955020](https://doi.org/10.1063/1.4955020).
- [49] T. Amotchkina, M. Trubetskov, D. Hahner and V. Pervak, *Characterization of e-beam evaporated Ge, YbF<sub>3</sub>, ZnS, and LaF<sub>3</sub> thin films for laser-oriented coatings*, Appl. Opt. **59**, A40 (2019), doi:[10.1364/AO.59.000A40](https://doi.org/10.1364/AO.59.000A40).
- [50] *Comsol multiphysic, v. 5.6* (2020), [www.comsol.com](http://www.comsol.com).
- [51] I. Colombo, J. Pedrini, E. Iemmolo and F. Pezzoli, *3D finite-element modeling of topological photonics in germanium*, Mater. Sci. Semicond. Process. **180**, 108539 (2024), doi:[10.1016/j.mssp.2024.108539](https://doi.org/10.1016/j.mssp.2024.108539).
- [52] J. D. Joannopoulos, *Photonic crystals: Molding the flow of light*, Princeton University Press, Princeton, USA, ISBN 9780691124568 (2008).

- [53] G. Dehlinger, L. Diehl, U. Gennser, H. Sigg, J. Faist, K. Ensslin, D. Grützmacher and E. Müller, *Intersubband electroluminescence from silicon-based quantum cascade structures*, *Science* **290**, 2277 (2000), doi:[10.1126/science.290.5500.2277](https://doi.org/10.1126/science.290.5500.2277).
- [54] D. J. Paul, *The progress towards terahertz quantum cascade lasers on silicon substrates*, *Laser Photonics Rev.* **4**, 610 (2010), doi:[10.1002/lpor.200910038](https://doi.org/10.1002/lpor.200910038).
- [55] W. P. Su, J. R. Schrieffer and A. J. Heeger, *Solitons in polyacetylene*, *Phys. Rev. Lett.* **42**, 1698 (1979), doi:[10.1103/PhysRevLett.42.1698](https://doi.org/10.1103/PhysRevLett.42.1698).
- [56] F. Liu and K. Wakabayashi, *Novel topological phase with a zero Berry curvature*, *Phys. Rev. Lett.* **118**, 076803 (2017), doi:[10.1103/PhysRevLett.118.076803](https://doi.org/10.1103/PhysRevLett.118.076803).
- [57] J. Zak, *Berry's phase for energy bands in solids*, *Phys. Rev. Lett.* **62**, 2747 (1989), doi:[10.1103/PhysRevLett.62.2747](https://doi.org/10.1103/PhysRevLett.62.2747).
- [58] W. A. Benalcazar, T. Li and T. L. Hughes, *Quantization of fractional corner charge in  $C_n$ -symmetric higher-order topological crystalline insulators*, *Phys. Rev. B* **99**, 245151 (2019), doi:[10.1103/PhysRevB.99.245151](https://doi.org/10.1103/PhysRevB.99.245151).
- [59] X. Ni, M. Weiner, A. Alù and A. B. Khanikaev, *Observation of higher-order topological acoustic states protected by generalized chiral symmetry*, *Nat. Mater.* **18**, 113 (2018), doi:[10.1038/s41563-018-0252-9](https://doi.org/10.1038/s41563-018-0252-9).
- [60] Y. Gong, S. Wong, A. J. Bennett, D. L. Huffaker and S. S. Oh, *Topological insulator laser using valley-Hall photonic crystals*, *ACS Photon.* **7**, 2089 (2020), doi:[10.1021/acsp Photonics.0c00521](https://doi.org/10.1021/acsp Photonics.0c00521).
- [61] M. I. Shalaev, W. Walasik, A. Tsukernik, Y. Xu and N. M. Litchinitser, *Robust topologically protected transport in photonic crystals at telecommunication wavelengths*, *Nat. Nanotechnol.* **14**, 31 (2018), doi:[10.1038/s41565-018-0297-6](https://doi.org/10.1038/s41565-018-0297-6).
- [62] A. B. Khanikaev and G. Shvets, *Two-dimensional topological photonics*, *Nat. Photon.* **11**, 763 (2017), doi:[10.1038/s41566-017-0048-5](https://doi.org/10.1038/s41566-017-0048-5).
- [63] B.-Y. Xie, H.-F. Wang, H.-X. Wang, X.-Y. Zhu, J.-H. Jiang, M.-H. Lu and Y.-F. Chen, *Second-order photonic topological insulator with corner states*, *Phys. Rev. B* **98**, 205147 (2018), doi:[10.1103/PhysRevB.98.205147](https://doi.org/10.1103/PhysRevB.98.205147).
- [64] L. Zhang et al., *Higher-order topological states in surface-wave photonic crystals*, *Adv. Sci.* **7**, 1902724 (2020), doi:[10.1002/advs.201902724](https://doi.org/10.1002/advs.201902724).
- [65] J. Bravo-Abad, A. Rodriguez, P. Bermel, S. G. Johnson, J. D. Joannopoulos and M. Soljacic, *Enhanced nonlinear optics in photonic-crystal microcavities*, *Opt. Express* **15**, 16161 (2007), doi:[10.1364/OE.15.016161](https://doi.org/10.1364/OE.15.016161).
- [66] F. Gao, H. Xue, Z. Yang, K. Lai, Y. Yu, X. Lin, Y. Chong, G. Shvets and B. Zhang, *Topologically protected refraction of robust kink states in valley photonic crystals*, *Nat. Phys.* **14**, 140 (2017), doi:[10.1038/nphys4304](https://doi.org/10.1038/nphys4304).